Journal of Materials Chemistry A

ROYAL SOCIETY OF CHEMISTRY

PAPER

View Article Online
View Journal | View Issue

Cite this: J. Mater. Chem. A, 2025, 13, 37297

Spontaneous cyclic transport mediated hydrovoltaic energy harvesting utilizing PB-PANI infused hierarchical porous wood structures†

Nazmul Hossain, *[a] Roozbeh Abbasi, [a] Weinan Zhao,[bc] Aiping Yu *[abc] and Norman Zhou *[ac]

Water evaporation, a crucial natural process, presents significant opportunities for sustainable energy production *via* hydrovoltaic technology. Nevertheless, actual implementations are hindered by insufficient energy output, complex fabrication processes, limited reliability, and high costs. This research presents a Cyclic Transport-Driven Hydrovoltaic Generator (CTHG), modeled after tree transpiration, which utilizes cyclic water flow to augment charge separation, stabilize voltage output, and enhance power density. The system reduces dependence on external water supplies while guaranteeing sustained operational stability, providing a scalable and effective option for renewable energy generation. This CTHG utilizes hierarchically porous delignified wood functionalized with Prussian blue (PB) nanoparticles and conductive polyaniline (PANI) as the medium for energy generation, enhancing water movement, electrical conductivity, and ion diffusion. Under ideal conditions, the device achieves a continuous voltage of 0.75 V, approximately twice the published average, and a power density of 6.75 μW cm^{-2} in deionized water. The voltage increases to 0.92 V in alkaline solutions at elevated temperatures with consistent performance observed over multiple days. Furthermore, series-connected CTHGs efficiently energize commercial devices, exemplified by illuminating an LED light with five units connected in series. This scalable, environmentally sustainable technique highlights the promise of bio-based materials for renewable energy production and wastewater reclamation, tackling significant worldwide energy issues.

Received 5th April 2025
Accepted 10th June 2025

DOI: 10.1039/d5ta02704g

rsc.li/materials-a

1. Introduction

Electricity generation from renewable energy sources, including wind, solar, hydro, and biomass, provides a sustainable and environmentally beneficial alternative to traditional fossil fuel-based energy.[1] Water has been extensively employed for hydropower, where potential energy is transformed into mechanical energy, they necessitate topographical characteristics and substantial infrastructure,[2] hence constraining their usability. Conversely, water evaporation—a fundamental process integral to energy transmission in environmental systems—has arisen as a feasible method for energy harvesting.[3] Recent breakthroughs in hydrovoltaic technology have shown energy generation *via* electrokinetic interactions between water and solid substances.[4,5] The phenomenon wherein water traverses limited channels within a material to generate electrical potential forms the basis for evaporation-driven electrical generators (EEGs), an innovative advancement in sustainable energy production[6,7] Enhancing EEG performance necessitates materials characterized by high porosity for effective water transport.[5,6,8,9] Extensive specific surface areas to improve solid–water interactions,[8] and plentiful functional groups to promote ion transport.[10] Wood, a readily accessible natural material, possesses a hierarchical cellular structure and remarkable hydrophilicity attributed to hydroxyl groups, rendering it a compelling option.[11,12] Balsa wood (Ochroma pyramidale) exhibits a distinctive amalgamation of low density, slender cell walls, and oriented micro/nano-fibrils, rendering it highly appropriate for EEG applications.[13] Delignification enhances wood's porosity and specific surface area, revealing functional groups that augment its ability for hydrovoltaic energy collection.[14] The inherent hierarchical porosity of wood offers a flexible foundation for the incorporation of functional materials and nanostructures, facilitating improved water evaporation and mass transfer efficiency.[15,16] Recent advancements have initiated the exploration of hydrovoltaic energy harvesting through natural evaporation in wood-based systems; however, only few studies have examined the integration of active materials into wood matrices for this application.[17,18] This study presents, for the first time, the functionalization of delignified

[a]Department of Mechanical and Mechatronics Engineering, University of Waterloo, Waterloo, ON, N2L 3G1, Canada. E-mail: nazmul.hossain@uwaterloo.ca; aipingyu@uwaterloo.ca; nzhou@uwaterloo.ca

[b]Department of Chemical Engineering, University of Waterloo, Waterloo, Ontario, N2L 3G1, Canada

[c]Waterloo Institute for Nanotechnology, University of Waterloo, Waterloo, Ontario, N2L 3G1, Canada

† Electronic supplementary information (ESI) available. See DOI: https://doi.org/10.1039/d5ta02704g

wood using nanostructured Prussian blue–polyaniline (PB-PANI) composites. This alteration enhances the electrical conductivity and water transport efficiency of the wood matrix, hence enabling more efficient conversion of evaporative energy into electricity.

The research, inspired by the natural transpiration mechanism in plants including evaporation through hierarchical porous structures, aims to produce functionalized wood-based evaporation-driven electrical generators.

A unique Cyclic Transport-Driven Hydrovoltaic Generator (CTHG) is presented to address the shortcomings of traditional unidirectional water flow systems. Cyclic water movement markedly improves charge separation by amplifying interactions between water molecules and material surfaces, thus enhancing voltage stability and power density.[14,19] This study presents a novel material platform and a unique design paradigm. The quasi-cyclic water flow—facilitated by deliberate evaporation, condensation, and capillary action within a semi-enclosed epoxy framework—significantly diminishes the necessity for active hydration while ensuring stable energy generation. This cyclic method decreases reliance on external water sources and alleviates surface charge saturation, hence providing sustained operating stability and longevity.[19,20] The CTHG represents a notable progression towards self-sustaining, low-carbon energy systems that can power small electronic devices. This innovation corresponds with the goals of renewable energy generation and resource sustainability.

2. Experimental section

2.1. Materials

Ammonium persulfate (APS), aniline (ACS, ≥99%), sodium chlorite ($NaClO_2$), hydrochloric acid (HCl), sodium hydroxide (NaOH), sodium chloride (NaCl), and magnesium chloride ($MgCl_2$), anhydrous ethanol solution (ACS, ≥99.5%), were obtained from Fisher Scientific. Prussian blue ($Fe_4[Fe(CN)_6]_3$) was acquired from Sigma-Aldrich Canada. Balsa wood samples were obtained from Thomes North America. Epoxy resin was purchased from Magic Resin.

2.2. Sample preparation

Balsa wood (BW) samples were cut into small pieces and further polished utilizing grinding and sanding techniques. To eliminate lignin, the samples were subjected to delignification in a 1 wt% sodium chlorite ($NaClO_2$) solution at 80 °C for 2 hours, followed by treatment in sodium hydroxide (NaOH) solutions at 80 °C for 20 minutes. The treated samples were further washed with acetone at 50 °C for 30 minutes to eliminate residual contaminants and improve their purity.

2.2.1. Synthesis of PB-PANI infused BW. 0.5 g of Prussian blue (PB) was subjected to sonication in 20 mL of a solution comprising ethanol and 1 M HCl for a duration of 3 hours. Thereafter, 0.93 mL of 99% aniline monomer was incrementally introduced to the solution and agitated with a magnetic stirrer for 30 minutes. Three pre-cut BW samples, totalling 4 g, were added to the resultant solution and refrigerated for 1 hour to produce the PB-aniline-BW samples. Separately, a solution of ammonium persulfate (APS) was prepared by gradually adding 2.3 g of APS in 1 M of 20 mL acetic acid (CH_3COOH) solution and kept in the refrigerator for 1 hour. This pre-cooled APS, which works as the oxidizing initiator, was slowly added dropwise to the previously prepared PB-aniline-BW solution over the course of 1 hour while maintaining continuous stirring in an ice bath at 3 ± 1 °C. Stirring continued for an additional 6 hours to ensure thorough polymerization, and finally washed and rinsed with alkaline solutions (1 M NaOH), DI water and ethanol. The samples were subsequently dried in a vacuum oven at 80 °C for 4 hours, resulting in a conductive PB-PANI-infused BW as shown in Fig. S1.† For comparison, pure PANI-infused BW was prepared through a similar procedure as above without the presence of Prussian blue (PB). Finally, the dried samples were cleaned with a plasma cleaner with O_2 for 2 minutes. Samples were named as D-BW (delignified balsa wood), PANI-BW (PANI infused balsa wood), and PB-PANI-BW (PB-PANI infused balsa wood).

2.3. Structural characterization

The surface morphology of the materials was analyzed utilizing an environmental scanning electron microscope (ESEM–Quanta FEG 250 ESEM, FEI, USA). Fourier-transform infrared (FTIR) spectroscopy (Bruker Tensor 27 FTIR spectrometer–PIKE Technologies, USA) equipped with an attenuated total reflectance (ATR)) was conducted within the range of 600–4000 cm^{-1} to ascertain surface functional groups. Hydrophilicity was assessed utilizing a water Contact Angle Instrument (Optical Contact Angle (OCA 35). Zeta potential was analyzed by Dynamic Light Scattering with Zeta Potential (Zetasizer Nano ZS). The materials' crystal structure was examined using X-ray diffraction (Bruker D8 Focus, Cu target). The specific surface area was assessed using multipoint BET techniques (Gemini VII 2390A, Micromeritics, USA). Samples were degassed at 90 °C for 12 hours in a nitrogen atmosphere before the surface area analyses. Thermogravimetric analyses (Q500, TA Instruments, USA) were performed on the wood-based samples in a nitrogen atmosphere throughout a temperature range from room temperature to 700 °C, heating rate 20 °C min^{-1}.

2.4. Electricity generation setup

High purity, flexible copper sheets were utilized as electrodes for the electrical performance assessments, forming a sandwich structure of copper-BW-copper. A 5 mL of DI water served as the water reservoir. The samples were connected to multimeter (Agilent 34411A, Keysight, USA), a SourceMeter (model B2901BL, Keysight, USA), or a Potentiostat/Galvanostat (Interface 1010 E, Gamry, USA) for various electrical measurements. The conclusions section should come in this section at the end of the article, before the acknowledgements.

3. Results and discussion

3.1. Design and characterization of the CTHG

Fig. 1(a) and S4† depicts the hierarchical structure of the Cyclic Transport-Driven Hydrovoltaic Generator (CTHG), consisting of a hydrophilic porous balsa wood (BW) layer enveloped in

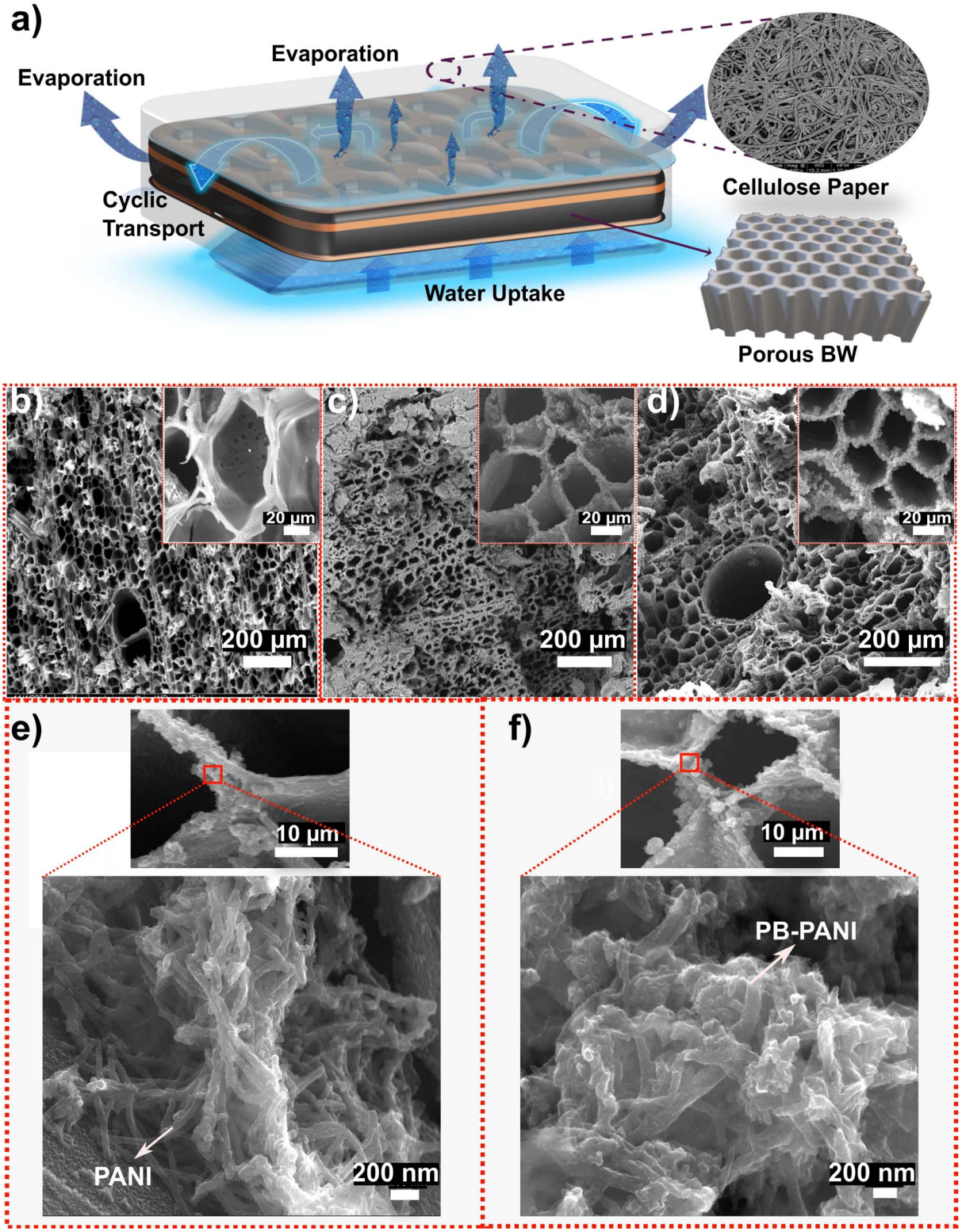

Fig. 1 (a) Schematic illustration of the CTHG device demonstrating water absorption, transportation, and evaporation, with inset highlighting the cellulose paper and balsa wood (BW) framework as the principal energy harvesting element. (b) SEM image of D-BW; (c) SEM image of PANI-BW; (d) SEM image of PB-PANI-BW. High-magnification SEM images depicting (e) PANI and (f) PB-PANI nanostructures on the BW surface.

cellulose paper and covered with a hydrophobic epoxy layer which works as holder. The BW layer, encased by cellulose paper, functions as the principal medium for water absorption, retention, and movement during the evaporation process. Water evaporation takes place through the strategically located windows in the outer epoxy enclosure, as shown in Fig. S4(c)

and S5(d and f).† This process generates a continuous upward water flow, with the hydrophilic cellulose layer promoting water absorption and transfer into the wood matrix. The epoxy shell, covering roughly 50% of the upper and lateral areas, improves mechanical integrity and facilitates internal condensation, whereas the exposed bottom surface (approximately 90%) enables effective water absorption from the reservoir. This configuration facilitates a quasi-cyclic hydration mechanism, in which capillary action and partial vapor condensation maintain moisture distribution within the porous matrix. The upward transport of water, driven by transpirational forces from surface evaporation, supports sustained device hydration, reduces external water needs in ambient environmental conditions.

The cohesive qualities of water, resulting from intermolecular forces, along with its adhesive contacts with cell walls, facilitate a continuous ascent through the structure. This efficient water transfer mechanism is essential to the operation of the ECG device.

The hierarchical design methodology, inspired by vascular plant structures, enables a mesoporous architecture featuring a comprehensive micro/nano channel network. Wood, recognized for its inherent capacity to facilitate and arrange water and nutrient transport in plants, is utilized for energy generation. Integrating PB-PANI into the cell walls establishes conductive pathways, noticeably augmenting surface area and improving charge transport for effective electricity generation. Here, water is initially absorbed by the cellulose paper and then transferred to the BW structure, which functions as the principal power-generating element. Water perpetually circulates through the cellulose paper, ascending from the bottom layer to the top through micro/nano-channels within the BW structure, while few portions of water is transferred directly through the cellulose paper to the top side of BW. Water circulates to the surroundings through the cellulose paper and BW. The quasi-cyclic water circulation in the CTHG system is primarily propelled by water loss *via* evaporation at certain evaporation windows and subsequent condensation on the inner surface of the epoxy enclosure. The continual phase transition process creates a dynamic wet–dry gradient that facilitates continuous water flow through the device. The hierarchically porous architecture of the wood facilitates spontaneous capillary-driven water transport, while the incorporation of cellulose paper improves both water absorption and ion conduction. The inherent anisotropic channels within the wood matrix enable unidirectional water movement, while the hygroscopic and porous characteristics of the cellulose paper covering enhance capillary wicking. Collectively, these attributes guarantee uniform hydration and directed water flow across the system. Experimental findings validated that water is effectively dragged from the bottom reservoir and redistributed through the bilayer structure *via* capillary action, maintained by evaporation-induced water loss.

Fig. 1(b)–(d) demonstrate the morphologies of delignified balsa wood (D-BW), polyaniline-infused balsa wood (PANI-BW), and Prussian Blue-Polyaniline-infused balsa wood (PB-PANI-BW), respectively. The delignification process removed lignin and hemicellulose, revealing micro- and nanoscale holes in the primary and secondary cell walls, along with the middle lamella (Fig. 1(b)). This structural alteration enhances the accessibility of cellulose fibrils, hence facilitating the interaction between capillary water movement or evaporation and the solid surface. The delignified wood demonstrated a well-maintained, interconnected hierarchical porosity structure, typical of its cellulose-rich composition, which promotes water movement and guarantees the even distribution of infused components. The incorporation of PANI and PB-PANI composites into the wood structure was clearly observed in the Fig. 1(e) and (f). Prussian Blue (PB) nanoparticles exhibited uniform distribution along the inner walls of the wood channels, whereas polyaniline (PANI) established a consistent coating layer, markedly enhancing the electrical conductivity of the material.

A synergistic composite is formed by *in situ* polymerization of pure PANI on the surface of delignified balsa wood (BW), and it appears as micro- and nanorod-like structure as observed in Fig. 1(e). PB-PANI has been integrated into the delignified balsa wood matrix to improve charge transport efficiency. The strong adherence of PB-PANI to the wood surface results from the uniform deposition of PB nanoparticles and the *in situ* growth of PANI nanorods, forming a three-dimensional interlinked network (Fig. 1(f)). This structure improves mechanical stability and reduces material degradation by securing conductive elements within the porous framework of the wood. The cross-sectional SEM analysis (Fig. S3†) demonstrated effective but uneven PB-PANI loading within vertically aligned BW channels, facilitating sustained water–solid interaction and continuous pathways for water and ion transport. Fourier-transform infrared (FT-IR) spectroscopy further confirmed the successful integration of PANI and PB into the wood matrix, validating the functionalization strategy. FT-IR spectra of D-BW, PANI-BW, and PB-PANI-BW were investigated to verify the incorporation of polyaniline (PANI) and Prussian blue nano structures on the BW structure, as shown in Fig. 2(a). The chemical composition of D-BW specimens was identified using FT-IR spectroscopy. Hemicellulose bands were seen at 1730 and 1240 cm^{-1} after chemical treatment, suggesting the removal of lignin.[21] Majority of the lignin and portion of hemicellulose was removed by the delignification process. In pure PANI-BW, the characteristic absorption bands at 1150 cm^{-1}, 1300 cm^{-1}, 1500 cm^{-1}, and 1590 cm^{-1} correspond to the C–H plane-bending vibration, C–N stretching vibration, C=C stretching of the benzenoid ring, and C=C stretching of the quinoid ring, respectively.[22] For PB-PANI-BW, characteristic vibrational peaks of PB were detected at about 2100 cm^{-1} which correspond to the stretching mode of the cyanide functional group (C≡N).[23] A broad absorption peak at around 3400 cm^{-1}, corresponding to antisymmetric and symmetric O–H stretching modes, together with a significant peak at 1650 cm^{-1}, linked to the H–O–H bending mode, indicates the presence of water molecules within the PB framework.[23,24] Fig. 2(b) exhibits the XRD patterns of D-BW, PANI-BW and PB-PANI-BW composites. The XRD profile of D-BW displays a large diffraction peak within the 2θ range of 17° and 23°, indicating that the removal of lignin did not damage the crystalline region of cellulose in the BW.[25] Whereas PANI-BW shows broad peak at 25° ascribed to the periodic parallel and

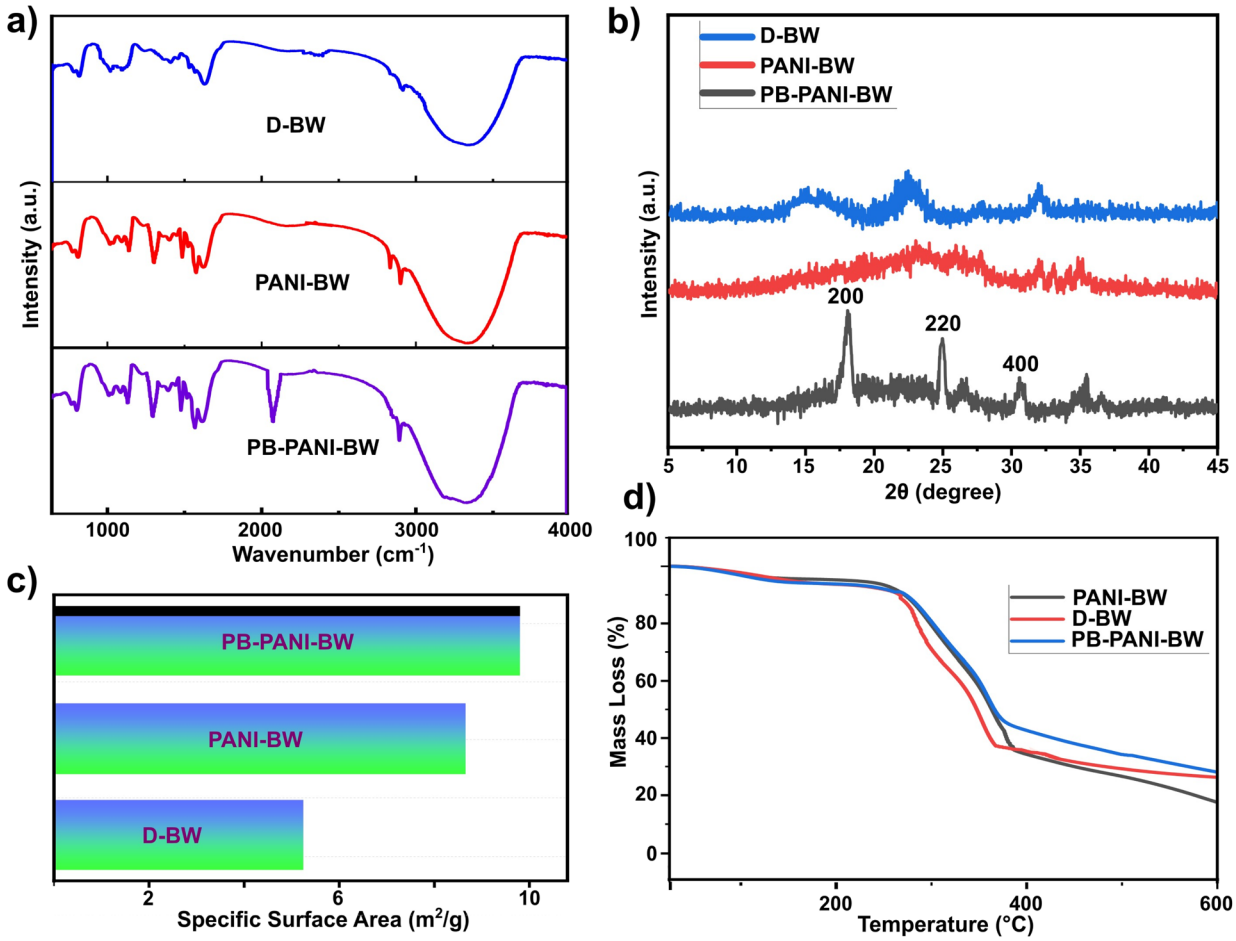

Fig. 2 (a) FTIR, (b) XRD, (c) SAA and (d) TGA results of delignified BW (D-BW), polyaniline infused balsa wood (PANI-BW), and Prussian blue-polyaniline infused balsa wood (PB-PANI-BW).

perpendicular alignment of PANI polymer chains.[26] This trait signifies the partly crystalline nature of PANI, in accordance with research.[27] The XRD pattern of PB-PANI-BW has three distinct peaks at 18°, 24°, and 33°, which correspond to the diffraction planes (200), (220), (400) of the PB-PANI crystalline structure,[28] that validates the successful integration of PB into the composite structure. The XRD analysis confirms the preservation of the wood's hierarchical structure post-functionalization, while the addition of PB-PANI enhances the crystallinity and structural properties of the composite material.

Fig. 2(c) confirms the BET specific surface area (SAA) of the 3 samples. Taking lignin out of native wood makes delignified balsa wood (D-BW) more porous and have a more surface area. The BET specific surface area (SSA) of D-BW reached 5.3 $m^2 g^{-1}$, which is higher than that of native balsa wood (BW), which is below 3 $m^2 g^{-1}$.[17,29] The addition of polyaniline (PANI) significantly improved the specific surface area (SSA), which rose to 8.1 $m^2 g^{-1}$, due to the development of PANI nanorods on the wood surface. The functionalization with Prussian blue-polyaniline (PB-PANI) composites resulted in an enhanced specific surface area (SSA) of 9.6 $m^2 g^{-1}$. The rise in SSA is probably attributable to the formation of microporosity, as corroborated by the SEM images. The increased specific surface area (SSA) facilitated more effective water transfer.

Thermogravimetric analysis (TGA) was performed to assess the thermal stability of these three samples. The TGA curves demonstrate a multi-stage weight loss process, with the early phase representing the evaporation of adsorbed moisture, succeeded by degradation stages linked to the dissolution of the structural backbone. The TGA profiles of BW, PANI-BW, and PB-PANI-BW exhibit slight weight reductions below 200 °C, ascribed to moisture evaporation and the elimination of low molecular weight oligomers. A notable mass loss transpires at around 265 °C, indicative of polymer chain breakdown and the ensuing burning of the carbon structure. Of the three samples, the PB-PANI-BW composite exhibits better thermal stability, signifying its increased resistance to heat degradation.

3.2. Water transport and distribution

CTHG device effectively transports water from the bottom reservoir to elevated regions by harnessing water potential, evaporation, and capillary action, without the aid of any external energy sources, as shown in Fig. 3(a). The water movement in the CTHG system aligns with the cohesion-

tension hypothesis,[30] where capillary forces and evaporation are the primary mechanisms driving water transport. Cohesive forces among water molecules, particularly enhanced by hydrogen bonding, are most pronounced near the air–water interface,[31] enabling efficient vertical flow through capillary action. These cohesive forces sustain a continuous column of water molecules, which are lifted by the tension generated through evaporation. The cross-sectional view of the device in Fig. 3(a) highlights the water uptake mechanism. As water evaporates through the designated openings, negative pressures (tension or suction) are generated. This tension enables the upward movement of water through the channels, akin to the process of drinking through a straw. Cohesion among water molecules ensures that, as the uppermost molecules are drawn to the surface, subsequent molecules follow, maintaining a steady flow.

Thin cellulose paper, exhibit high porosity and permeability to water, facilitating rapid water transfer upon initial contact. This cellulose layer transfers water to the bottom layer of the PB-PANI-BW structure, with some portion distributed to the upper and surrounding sections of the structure as shown in Fig. S4.† Water subsequently rises through the permeable wood

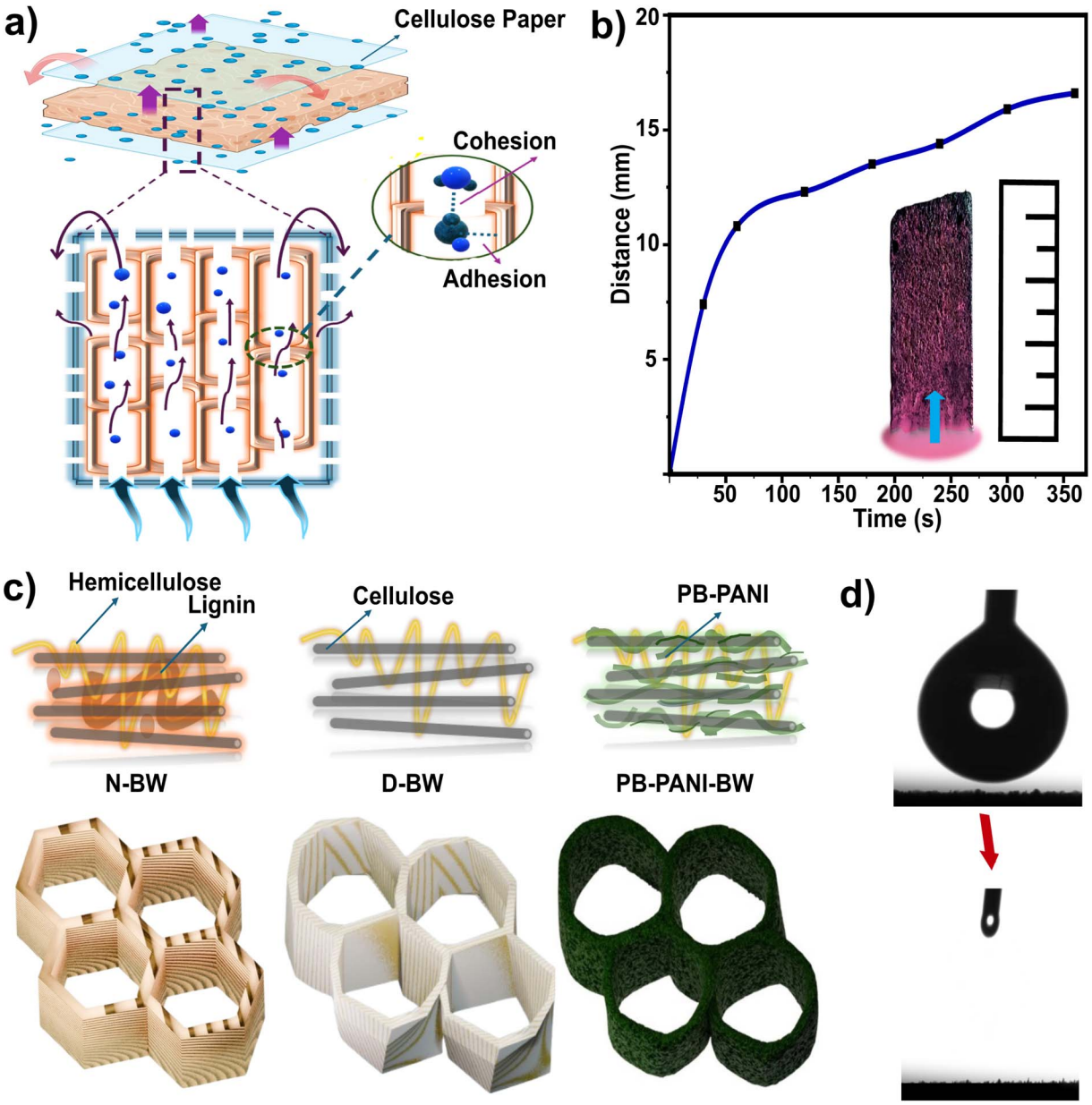

Fig. 3 (a) Schematic illustration of water transport *via* the CTHG system, inset depicting the cross section of the system where water flowing through the micro/nano channels. (b) Subsequent variation of water flow distance in the PB-PANI-BW system along the longitudinal axis. (c) Schematic representation of the preparation process for PB-PANI-BW, progressing from native wood (N-BW) to delignified wood (D-BW) to PB-PANI-BW, along with associated alterations in cell-wall structure. (d) Measurement of the contact angle for PB-PANI-BW, demonstrating a very hydrophilic surface.

structure *via* micro/nano channels acting as capillaries, reaching the upper cellulose paper layer through a structured network of pathways. Evaporation from the wood/cellulose paper structure results in water loss, similar to plant transpiration, with the water potential nearing $\Psi_p = 0$ MPa at the wilting threshold, counterbalanced by absorption from the reservoir.[32] The varied exposure of the BW structure produces differential evaporation rates, creating a water concentration gradient that influences transport dynamics. Continuous water migration from the paper to the wood structure occurs through osmosis, driven by the lower solute potential (Ψ_s) of the PB-PANI-BW structure relative to the reservoir due to the higher solute concentration imparted by polyaniline (PANI). This solute potential differential ensures the ongoing influx of water into the BW structure, with water moving through both cell walls and channels. The present design utilizes a hierarchical methodology to enhance water transport kinetics by evaporation. Water transport over time for the PB-PANI-BW structure, in the absence of both the cellulose paper wrapping and the epoxy enclosure, is presented in Fig. 3(b). The impact of differing temperature and relative humidity on this transport pattern is further depicted in ESI Fig. S8.† Balsa wood (BW) is predominantly composed of cellulose, hemicellulose, and lignin (Fig. 3(c)). Employing wood nanotechnology, lignin and hemicellulose were selectively extracted, resulting in delignified wood (DW) characterized by a mesoporous and hierarchical architecture. This alteration, defined by micro- and nanoscale channels, maintained the inherent cell wall structure while increasing porosity and improving water absorption, hence augmenting the system's efficiency for water transport (Fig. 3(c)). The hierarchical architecture, which includes interlamellar pores in PB-PANI and intrinsic micropores within the wood vessels and lumens, improves water responsiveness as illustrated in Fig. 3(c). The improved hydrophilicity and structural anisotropy of the channels in PB-PANI-BW enables unidirectional, pump-free water transport driven by capillary forces, leading to an increased water transport rate. Moreover, water contact angle measurement (Fig. 3(d)) confirms the hydrophilicity of the PB-PANI-BW system. Observations indicate the surface's substantial hydrophilicity, promoting swift water absorption (S-V1).

3.3. Water-induced electricity generation *via* interfacial evaporation

While CTHG device is submerged in water, it achieves a balance between water absorption at the base and evaporation at the top and sides as shown in Fig. 4(a) and S4.† BW piece is encased in cellulose paper and affixed to a copper sheet for energy harvesting. This anisotropic device, encapsulated in an epoxy resin framework effectively transforms water flow and evaporation into electrical energy, providing a cost-efficient and durable alternative for sustainable energy harvesting. The generation of voltage in this system can be ascribed to the movement of water through the mesoporous BW, facilitated by various factors. The hydroxide ions in the water and the conductive PB-PANI material encounters repulsive forces due to their similar charges, leading to the directional migration of hydrogen ions illustrated in Fig. 4(a) inset. The ion flow produces a quantifiable voltage and current, which is measured by using a source meter. The effectiveness of the CTHG device is assessed under uniform environmental circumstances utilizing three formats of BW. D-BW yields the lowest voltage (~427 mV); however, PANI-infused balsa wood (PANI-BW) generates 610 mV, and PB-PANI-infused balsa wood (PB-PANI-BW) achieved the highest voltage of 751 mV as seen in Fig. 4(b). The current also shows similar trend as shown in Fig. 4(c). The incorporation of polyaniline (PANI), a conductive polymer, into the cellulose matrix created a continuous conductive network, thereby improving ion mobility and offering electroactive sites for enhanced charge separation and transfer. The integration of Prussian Blue (PB), a redox-active super capacitive material, enhanced the device's energy harvesting capabilities by augmenting charge storage, enlarging the effective surface area, and optimizing electron and ion transport properties. The combined effects of delignification, PANI, and PB markedly enhanced the voltage and current outputs of the device (Fig. 4(b) and (c)). This hierarchical design illustrates scalability and usability for hydrovoltaic energy harvesting, establishing the device as a viable solution for low-power environmental sensors and small electronic applications. This behaviour can be elucidated by the streaming potential (V_s) and streaming current (I_s) process, as delineated in eqn (1) and (2):

$$V_s = \frac{4\varepsilon_0\varepsilon_r\gamma\zeta\cos\theta}{\sigma\mu d} \quad (1)$$

$$I_s = \frac{\Pi\varepsilon_0\varepsilon_r d\gamma\zeta\cos\theta}{\mu L} \quad (2)$$

where d refers to the aperture of the capillary channel; θ is the contact angle between water and capillary; γ is the surface tension of water; L the length of the capillary, and the inner surface zeta potential ζ are known.

Several polar functional groups, including hydroxyl, carboxyl, sulfonated, and amine groups were introduced by the delignification procedure.[33,34] The polar functional groups in Prussian Blue (such as cyanide (–CN), hydroxyl (–OH), and adsorbed water) and polyaniline including amine (–NH–), imine (–N=), and protonated amine ($-NH_2^+$)[35] engages with water to dissociate H^+ ions and promotes robust chemical interactions, hence improving stability and electrochemical performance. The hierarchical and porous architecture of PB-PANI-BW establishes interconnected channels that improves water droplet sensitivity and charge carrier collection, hence augmenting energy generation. These polar functional groups interact with water molecules, causing the dissociation of H^+ ions and resulting in increased concentration gradients, therefore augmenting the voltage output. The establishment of the electrical double layer (EDL) enables selective ion transport, resulting in an asymmetric ion distribution and generating a voltage differential between the upper and lower surfaces. The hierarchical structure of PB-PANI-BW facilitates swift water passage *via* cellulose micro/nanofibrils, hence enhancing charge production. The gradient of water content within the

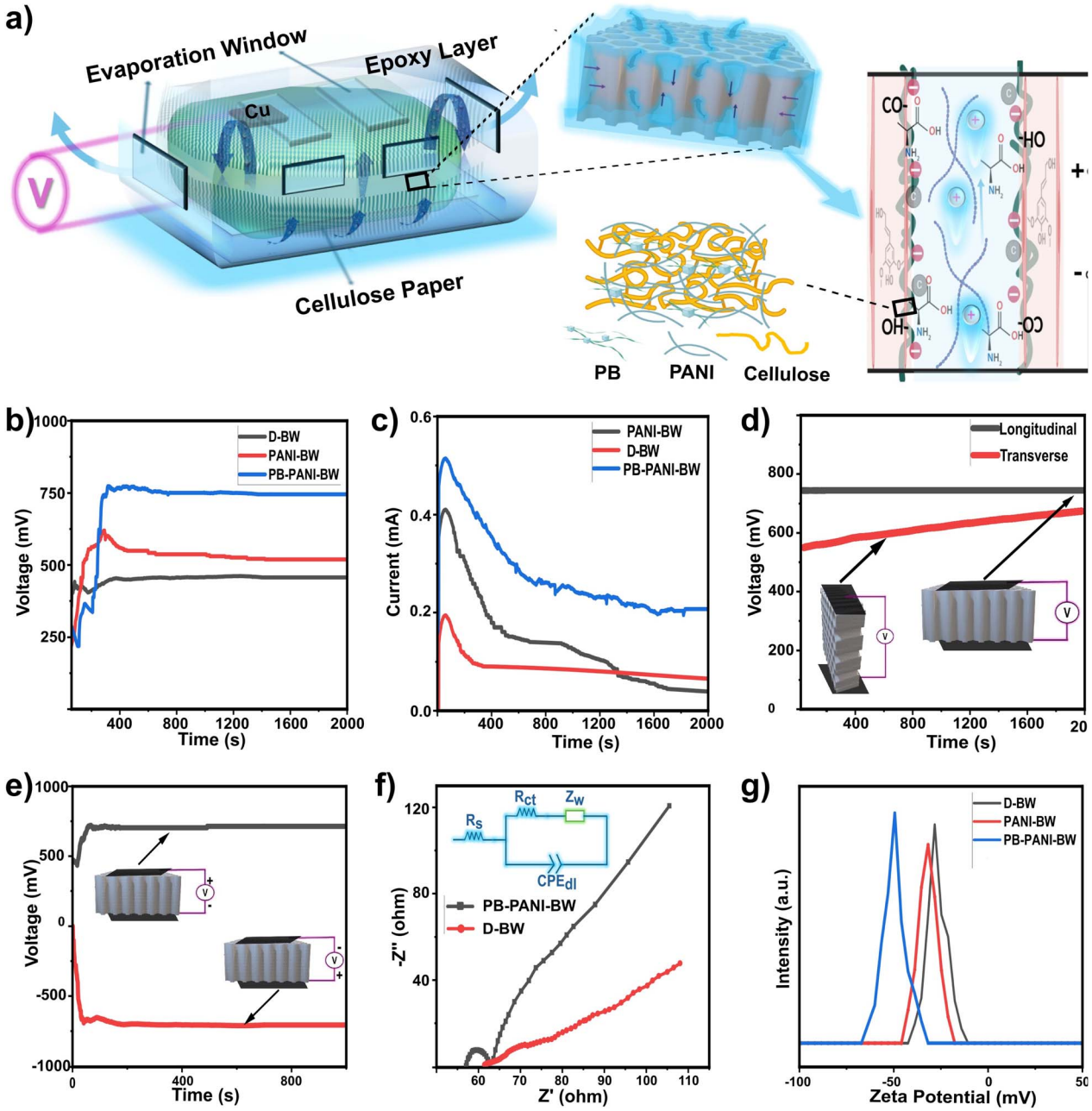

Fig. 4 (a) Schematic illustration of energy harvesting from the CTHG device through water evaporation, inset depicting cyclic water transport through the channels, mechanisms of streaming potential for voltage generation, and the nanostructure configurations of PB and PANI on the cellulose matrix of wood. (b) Open circuit voltage generation and (c) short circuit current output from D-BW, PANI-BW, and PB-PANI-BW. (d) Open-circuit voltage generation in the longitudinal and transverse orientations. (e) Open-circuit voltage response when reversing the positive and negative electrodes while maintaining circuit continuity. (f) Nyquist plot for D-BW, PANI-BW, and PB-PANI-BW. (g) The zeta potential of the respective BW samples.

paper/wood structure induces asymmetric adsorption of positive counterions, resulting from the balance between capillary flow and evaporation. This creates a potential differential between the wet and dry areas, determined by fluctuations in surface charge density (σ). As a result, a voltage is generated across the structure due to uneven ion adsorption which is illustrated in Fig. S11 and S12.† The movement of positive ions through capillary flow modifies the potential gradient within the electric double layer (EDL). Consequently, electrons on the conduction band surface migrate in reaction to the positive ion movement to uphold charge neutrality, producing a current referred to as pseudostreaming.[36,37]

Furthermore, the PB-PANI network within the cell walls reinforced the composite structure, enhancing its durability over time. The alignment of the PB-PANI-BW considerably influences its performance. The voltage generated in the

transverse direction is lower than in the longitudinal direction (Fig. 4(d)). In the transverse orientation, there is restricted water diffusion due to the alignment of the cell walls. In contrast, the hierarchical, aligned structure in the longitudinal direction facilitated more efficient water transport and ion diffusion, resulting in elevated voltage. The device design used a hydrophobic epoxy layer with an evaporation window to improve mechanical stability and evaporation efficiency. The incorporation of Prussian blue-polyaniline composite distinguished by its extensive specific surface area and functional groups that strongly adsorb water, enhanced the hydrovoltaic effect by facilitating efficient charge transfer among water, PB-PANI-BW, and cellulose paper. Negative surface charges from hydrophilic functional groups in BW, PANI, and PB increased the surface charge density, hence promoting greater voltage generation.

The results indicate the feasibility of integrating delignified wood, conductive polymers–PANI, and Prussian blue (PB) structures for effective and sustainable hydrovoltaic energy generation. The passage of ions produces a current during flow, with an elevated potential on the upper surface, leading to a substantial open-circuit voltage. Reversing the device's orientation results in an inversion of voltage polarity while preserving the same magnitude (Fig. 4(e)), illustrating the device's bidirectional functionality.

The CTHG device utilizes the inherent micro/nanochannel structure and anisotropic characteristics of wood to enable hydrovoltaic energy generation. As water traverses the channels, negatively charged surfaces provoke the migration of positive charges, leading to a potential difference across the material. The principal mechanisms facilitating hydrovoltaic power generation are the streaming potential produced by charged fluid movement in nanochannels[38] and the ionovoltaic effect at the liquid–solid interface, wherein charge interactions at the electric double layer (EDL) generate electric current.[39] Electrochemical Impedance Spectroscopy (EIS) was utilized to examine the electrochemical characteristics of BW and PB-PANI-BW composites. The Nyquist plots (Fig. 4(f)) exhibited a semicircular arc in the high-frequency domain and an oblique line in the low-frequency domain for PB-PANI-BW indicating the presence of both capacitive and diffusive mechanism. The associated equivalent circuit model is illustrated in the inset of Fig. 4(f). Conversely, the D-BW sample exhibits an oblique line, indicative of diffusion-dominated behaviour, where the solution resistance (R_s) measured at 61.94 Ω, while the charge transfer resistance (R_{ct}) was recorded at 53.45 Ω. The semicircle's diameter represents the charge transfer resistance, whereas its intersection with the real axis signifies the series resistance. The behaviour of curve indicates that PB-PANI-BW has lower resistance and enhanced conductivity that signifies enhanced charge transfer at solid–liquid interface comparing with D-BW. Zeta potential tests were performed to assess the surface charge properties of DW, PANI-BW, and PB-PANI-BW in aqueous solutions (Fig. 4(g)). The zeta potential of D-BW was −27 mV. The modification with PANI elevated the potential to +36 mV, indicating a substantial enhancement in surface charge attributable to the incorporation of polyaniline, which facilitates the development of an electric double layer (EDL) on the wood surface. The use of PB further augmented the surface charge to −53 mV, signifying greater electrostatic interactions essential for effective energy generation.

This capillary-driven transport enables a steady ion flow across the cellulose paper and wood composite, promoting effective charge separation within the entire structure. The resulting ionic movement produces a measurable electric potential, validating the hydrovoltaic energy harvesting technique. The interaction between material structure, moisture dynamics, and surface functionality is essential for achieving stable and enhanced energy output in ambient environmental conditions.

3.4. Environmental effect on the electrical performance

The effectiveness of Cyclic Transport-Driven Hydrovoltaic Generators (CTHGs) is markedly affected by environmental factors including humidity, temperature, solution composition, NaCl content, wind velocity, and light intensity. A comprehensive assessment of these elements was performed to ascertain their influence on the generator's electrical performance.

In environments with high humidity, the evaporation rate was observed to decrease, which subsequently resulted in diminished device performance at 80% relative humidity (RH) (Fig. 5(a)). On the other hand, elevating the water reservoir temperature from room temperature to 70 °C led to a steady increase in the open-circuit voltage (V_{OC}), which peaked at 880 mV at 70 °C (Fig. 5(b)). In a similar manner, as the ambient temperature rose from room temperature to 50 °C, the voltage exhibited an increase to 0.78 V (Fig. 5(b)). This improvement is linked to the increased migration speed of water molecules at higher temperatures, enabling more effective charge separation.[40] Nonetheless, increased temperatures lead to a faster rate of water evaporation, which enhances the voltage.[41] This phenomenon is associated with the interplay of accelerated water molecule movement, heightened evaporation rates, and thermoelectric influences. At lower temperatures, specifically around 0 °C, the decrease in voltage can be attributed to diminished evaporation rates and the slower movement of water molecules, consistent with theoretical predictions.[42]

The device's efficacy fluctuated among various electrolytic solutions. Concentrated chloride solutions demonstrated superior voltage outputs relative to diluted ones, with the maximum output recorded in the NaCl solution (Fig. 5(c)). The ionic concentration in the solutions enhanced charge transfer and separation, markedly increasing V_{OC} and I_{SC}. The concentration of NaCl was a pivotal component. At 1 M NaCl, the CTHG attained optimal performance with a V_{OC} of 910 mV and an I_{SC} of 0.46 mA (Fig. 5(d)). Elevated ionic strength in the solution augmented electrokinetic interactions and ion transport.

The voltage output escalated with air speed, attaining a maximum of 0.79 V at 6 ms^{-1} (Fig. 5(e)). Increased evaporation rates in windy conditions enhanced charge separation, guaranteeing enhanced performance. Similarly, light exposure significantly influenced device performance. Increased light exposure enhanced the evaporation rate, with the peak voltage seen at a light intensity of 10 000 lux (Fig. 5(f)). This underscores

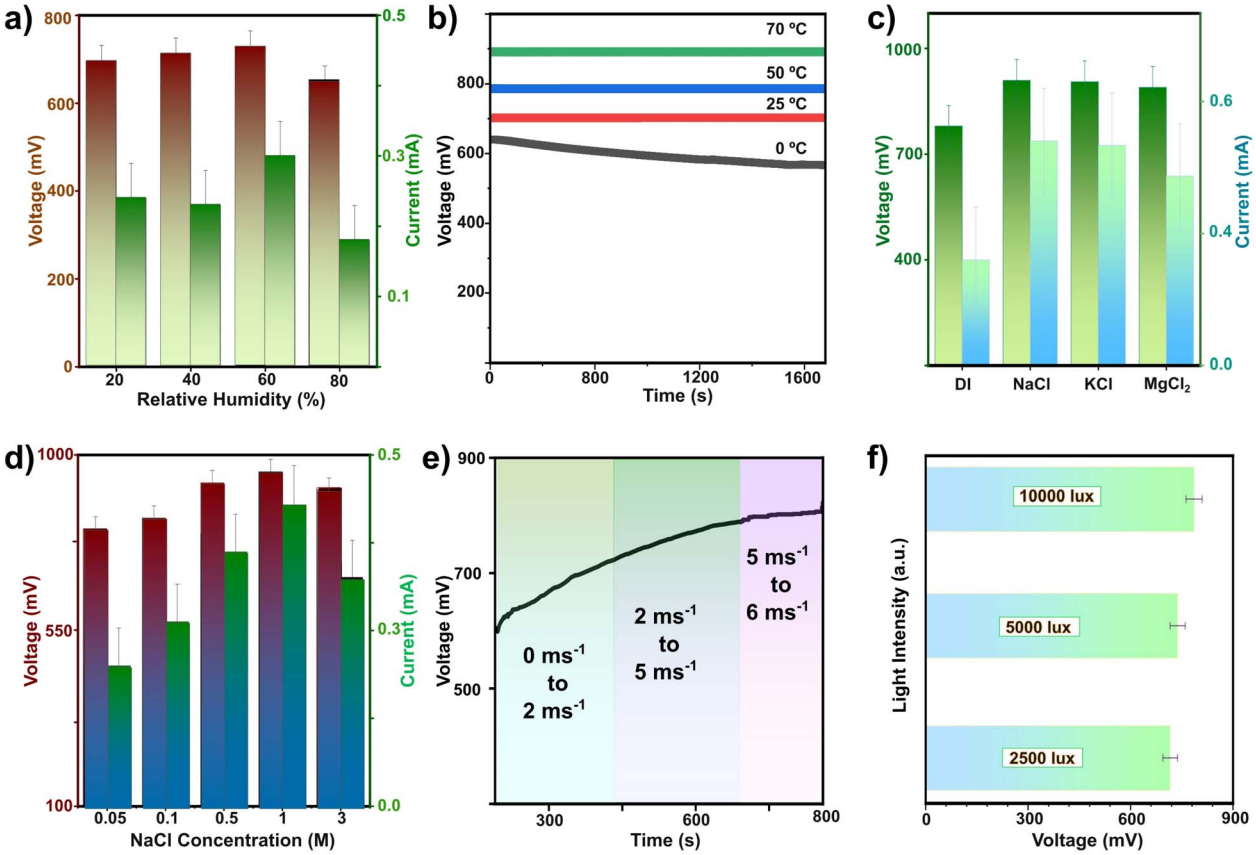

Fig. 5 The influence of diverse environmental and experimental variables on the open-circuit voltage and short-circuit current of the system, including (a) relative humidity, (b) temperature, (c) various solution types, (d) NaCl concentration, (e) wind speed, and (f) light intensity.

the potential of CTHGs for utilization in sunlight-abundant settings. CTHGs provide consistent, scalable, and reusable performance affected by environmental variables such as temperature, humidity, and light, hence improving energy harvesting efficiency. Their versatility underscores prospective uses in sustainable energy generation and environmental investigation.

3.5. Exploring scalability and application potential of CTHG device

To augment the output power of Cyclic Transport-Driven Hydrovoltaic Generator (CTHG), multiple CTHG devices are connected in series and parallel, similar to conventional batteries. Fig. 6(a) depicts the peak voltage and current outputs for several series and parallel connection setups. The voltage and current demonstrate a nearly linear increase with the number of samples arranged in series or parallel. Connected 4 CTHG devices in series generates a voltage of 2.68 V (Fig. 6(a)), whereas 4 CTHGs connected in parallel attained a value of 1.65 mA. Additionally, 2 sets of series and parallel connection generates a voltage of 1.41 V and current of 0.83 mA, demonstrating the device's capability for scalability regarding voltage and current production. The evaluation of the power output from the CTHG was conducted across various load resistances, as illustrated in Fig. 6(b). The maximum power output was measured at approximately 6.8 μW cm^{-2} with a load resistance of about 10 000 Ω. The CTHG demonstrated the ability to charge a 470 μF capacitor to 0.75 V in less than 180 seconds (Fig. 6(c)), reflecting the generator's ability to charge a capacitor. Additionally, the connection of five CTHG units in series successfully powers an LED light with aid of a capacitor, as shown in Fig. 6(d). The capacitor was used for voltage stability. The video (S-V2) offers additional insights into the LED lighting demonstration that is powered by five CTHG units.

Fig. 6(e) illustrates that substituting deionized water with tap water, rainwater, and NaOH solutions led to increased voltage outputs. The ionic content of tap water enabled effective charge separation and transport, while rainwater demonstrated moderate performance attributed to its slightly reduced ionic concentration. The addition of NaOH solutions resulted in a notable increase in power output, which can be attributed to enhanced ionic conductivity and strong electrokinetic interactions. In contrast, deuterium oxide (D_2O) demonstrated decreased efficiency, which can be linked to changes in hydrogen bonding and a reduction in ion diffusion rates, although it continued to function effectively.[57] The performance of the CTHG is systematically compared with other advanced porous materials, as illustrated in Fig. 6(f). The CTHG utilizing PB-PANI-BW demonstrated superior performance compared to previously reported devices, achieving nearly double the average

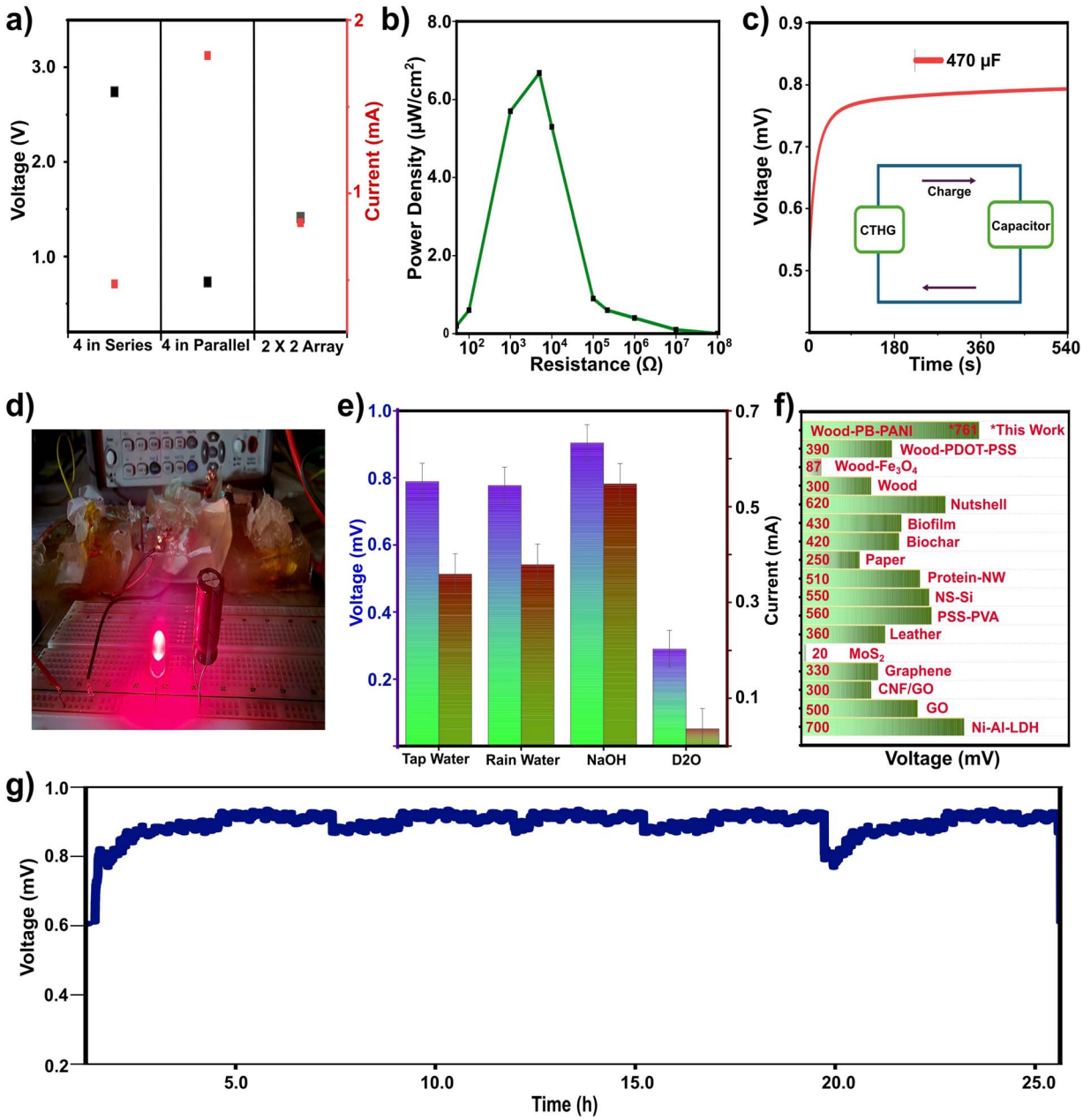

Fig. 6 (a) Open circuit voltage and short circuit current characteristics of PB-PANI-BW based CTHG device samples connected in series and parallel. (b) Output power density of the PB-PANI-BW based CTHG device as a function of varying external load resistance. (c) Supercapacitor charging curve with deionized water. (d) Voltage output from five PB-PANI-BW based CTHG device connected in series to power an LED. (e) Voltage generation from various practical solutions, including tap water, rainwater, alkaline solution, and heavy water (deuterium oxide). (f) Comparative analysis of voltage generation by PB-PANI-BW based CTHG device with other hydrovoltaic devices reported in the literature,[33,43–56] (g) Voltage generation at 30 °C in alkaline solutions over 25 hours.

performance of other devices referenced in the literature.[51] The long-term stability of the device is assessed in alkaline solutions (NaOH) at 30 °C. Fig. 6(g) shows the recorded average voltage over a duration of 25 hours is 0.92 V. This elevation of voltage is due to significant potential difference which is triggered by the substantial evaporation rate and concentration gradient. Following five days cycles within a week, the CTHG sustained its voltage (Fig. S13†). The results indicate the device's consistent performance and long-term reliability.

4. Conclusions

This study presents a novel Cyclic Transport-Driven Hydrovoltaic Generator (CTHG), drawing inspiration from the natural transpiration process in trees, aimed at overcoming the constraints of conventional unidirectional systems. The CTHG utilizes a cyclic water flow mechanism to improve charge separation, maintain stable voltage output, and boost power density, all while minimizing reliance on external water

reservoir and ensuring extended operational stability. This CTHG system incorporates hierarchically porous balsa wood structure that is functionalized with Prussian blue nanoparticles and conductive polyaniline polymers, aiming to enhance water transport, ion diffusion, and selective ion transport across nonuniform electric double layers in micro- and nanochannels. The PB-PANI-BW, created by infusing a hierarchical BW template with PB-PANI, exhibits a fibrous network and a large specific surface area, promotes effective ion transport and evaporation-driven electricity production, attaining an open-circuit voltage of 0.76 V and a power density of 6.75 $\mu W\ cm^{-2}$, while maintaining stable performance for over 25 hours. The connection of five CTHG units in series resulted in a combined output voltage over 3 V, which is adequate for powering any small electronics devices. The power generating efficacy was affected by environmental variables like temperature, humidity, wind velocity, and light intensity; yet the device continued to function under outdoor settings. This study emphasizes the promise of bio-based materials in sustainable energy, utilizing wood's hierarchical structure and enhanced functionalization for scalable solutions in renewable energy and water sustainability.

Data availability

The data supporting the findings of this study can be obtained from the corresponding author upon request.

Author contributions

Nazmul Hossain–conceptualization, data acquisition, and original draft writing; Roozbeh Abbasi and Weinan Zhao–validation and proof reading; Aiping Yu and Norman Zhou–review and supervision.

Conflicts of interest

The authors declare that they have no known competing financial interests or personal relationships that could have appeared to influence the work reported in this paper.

Acknowledgements

This work is supported by NSERC, CRC, Mitacs, AquaSensing and University of Waterloo.

References

1 K. K. Jaiswal, C. R. Chowdhury, D. Yadav, R. Verma, S. Dutta, K. S. Jaiswal, B. Sangmesh and K. S. K. Karuppasamy, *Renewable and Sustainable Clean Energy Development and Impact on Social, Economic, and Environmental Health*, Vol. 7, Elsevier Ltd, 2022.

2 D. Malovic, H. Engelmann-Pilger, N. Arsenijevic, K. B. Gassner, E. Merle-Beral, G. Monti, J. Pooley, L. K. Inouye, J. Levin and J. Kellenberg, *Hydroelectric power : a guide for developers and investors (English)*, World Bank Group, Washington, D.C., 2015, http://documents.worldbank.org/curated/en/917841468188335073.

3 A. Yaroshchuk, *Evaporation-driven Electrokinetic Energy Conversion: Critical Review, Parametric Analysis and Perspectives*, Vol. 305, Elsevier B.V., 2022.

4 C. Zheng, W. Chu, S. Fang, J. Tan, X. Wang and W. Guo, *Interdiscip. Mater.*, 2022, **1**, 449.

5 L. Li, X. Wang, W. Deng, J. Yin, X. Li and W. Guo, *Hydrovoltaic Energy from Water Droplets: Device Configurations, Mechanisms, and Applications*, Vol. 2, John Wiley and Sons Inc, 2023.

6 M. S. Kang, H. Ko, S. Lee and S. B. Cho, *J. Phys. Chem. C*, 2023, **127**, 16811.

7 X. Zhang, X. Zhang, X. Fan, H. T. Ren, J. H. Lin, C. W. Lou and T. T. Li, *J. Mater. Chem. A*, 2023, **11**, 26173.

8 S. Jiao, Y. Zhang, Y. Li, B. Maryam, S. Xu, W. Liu, M. Liu, J. Li, X. Zhang and X. Liu, *Polymers*, 2023, **15**, 4079.

9 J. Tan, S. Fang, Z. Zhang, J. Yin, L. Li, X. Wang and W. Guo, *Nat. Commun.*, 2022, **13**, 3643.

10 S. L. Gong, Y. C. Tian, G. P. Sheng and L. J. Tian, *Nat. Commun.*, 2024, **15**, 4365.

11 M. Tang, X. Fang, B. Li, M. Xu, H. Wang and S. Cai, *Polymers*, 2022, **14**, 2077.

12 A. Kumar, T. Jyske and M. Petrič, *Delignified Wood from Understanding the Hierarchically Aligned Cellulosic Structures to Creating Novel Functional Materials: A Review*, Vol. 5, John Wiley and Sons Inc, 2021.

13 M. Borrega, P. Ahvenainen, R. Serimaa and L. Gibson, *Wood Sci. Technol.*, 2015, **49**, 403.

14 P. Grönquist, M. Frey, T. Keplinger and I. Burgert, *ACS Omega*, 2019, **4**, 12425.

15 Y. Lu, D. Fan, Z. Shen, H. Zhang, H. Xu and X. Yang, *Nano Energy*, 2022, **95**, 107016.

16 X. Wang, X. Xu, D. Fan, G. Zhang and Y. Lu, *Review: Wood Composites as Sustainable Energy Conversion Materials for Efficient Solar Energy Harvesting and Light Management*, Vol. 59, Springer, 2024, pp. 4383–4403.

17 C. Wang, S. Tang, B. Li, J. Fan and J. Zhou, *Chem. Eng. J.*, 2023, **455**, 140568.

18 Y. Gao, X. Yang, J. Garemark, R. T. Olsson, H. Dai, F. Ram and Y. Li, *ACS Sustain. Chem. Eng.*, 2023, **11**, 11099.

19 M. Kaur, S. Ishii, R. Nozaki and T. Nagao, *Sci. Rep.*, 2021, **11**, 10954.

20 J. Chung, D. Heo, G. Shin, S. H. Chung, J. Hong and S. Lee, *Nano Energy*, 2021, **82**, 105687.

21 Y. Horikawa, S. Hirano, A. Mihashi, Y. Kobayashi, S. Zhai and J. Sugiyama, *Appl. Biochem. Biotechnol.*, 2019, **188**, 1066.

22 Y. Jiao, C. Wan and J. Li, *J. Mater. Sci.: Mater. Electron.*, 2017, **28**, 2634.

23 A. M. Nawar and A. A. Alzharani, *Mater. Chem. Phys.*, 2023, **306**, 128000.

24 A. M. Farah, C. Billing, C. W. Dikio, A. N. Dibofori-Orji, O. O. Oyedeji, D. Wankasi, F. M. Mtunzi and E. D. Dikio, *Int. J. Electrochem. Sci.*, 2013, **8**, 12132.

25 F. Lionetto, R. Del Sole, D. Cannoletta, G. Vasapollo and A. Maffezzoli, *Materials*, 2012, **5**, 1910.

26 K. T. Vadiraj and S. L. Belagali, *IOSR J. Appl. Chem.*, 2015, **08**, 53.
27 A. N. J. Al-Daghman, *Int. J. Res. Appl. Sci. Eng. Technol.*, 2018, **6**, 1555.
28 Y. Luo, L. Yang, Q. Liu and Y. Yan, *R. Soc. Open Sci.*, 2021, **8**, 211092.
29 Y. Meng, Y. Jiang, Y. Chen and J. Zhang, *Polymers*, 2024, **16**, 3213.
30 F. W. Bentrup, *Water Ascent in Trees and Lianas: the Cohesion-Tension Theory Revisited in the Wake of Otto Renner*, Vol. 254, Springer-Verlag Wien, 2017, pp. 627–633.
31 F. Baluškabaluška and J. Vivanco, *Signaling and Communication in Plants Series*, 2011, vol. 234, pp. 205–211.
32 Y. Chen, J. Yang, D. Zhang, S. Wang, X. Jia, Y. Li, D. Shao, L. Feng, H. Song and S. Tang, *J. Mater. Chem. A*, 2023, **11**, 2349.
33 J. Lin, Z. Zhang, X. Lin, X. Cai, S. Fu, X. Fang, Y. Ding, X. Wang, G. Sèbe and G. Zhou, *Adv. Funct. Mater.*, 2024, 2314231.
34 F. Kačík, J. Luptáková, P. Šmíra, A. Nasswettrová, D. Kačíková and V. Vacek, *Bioresources*, 2016, **11**, 3442.
35 X. Zhang, C. Sui, J. Gong, R. Yang, Y. Luo and L. Qu, *Appl. Surf. Sci.*, 2007, **253**, 9030.
36 C. Ge, D. Xu, X. Feng, X. Yang, Z. Song, Y. Song, J. Chen, Y. Liu, C. Gao, Y. Du, Z. Sun, W. Xu and J. Fang, *Nano-Micro Lett.*, 2025, **17**, 29.
37 Y. Zhang, T. Yang, K. Shang, F. Guo, Y. Shang, S. Chang, L. Cui, X. Lu, Z. Jiang, J. Zhou, C. Fu and Q. C. He, *Nat. Commun.*, 2022, **13**, 3484.
38 K. Jiao, B. Ma, X. Liu, B. Chen, Q. Wang and C. Zhao, *Advances in 3D Materials-Based Hydrovoltaic Generators and Synergistic Energy Conversion*, John Wiley and Sons Inc, 2024.
39 W. H. Lee, J. Park, S. G. Yoon, H. Jin, J. Han and Y. S. Kim, *Ionovoltaics in Energy Harvesting and Applications: A Journey from Early Development to Current State-Of-The-Art*, Vol. 5, John Wiley and Sons Inc, 2023.
40 Y. Hu, W. Yang, W. Wei, Z. Sun, B. Wu, K. Li, Y. Li, Q. Zhang, R. Xiao, C. Hou and H. Wang, *Phyto-inspired Sustainable and High-Performance Fabric Generators via Moisture Absorption-Evaporation Cycles*, Vol. 10, 2024.
41 F. Yu, J. Li, Y. Jiang, L. Wang, X. Yang, Y. Yang, X. Li, K. Jiang, W. Lü and X. Sun, *Advanced Science*, 2023, **10**, 2302941.
42 L. Li, X. Wang, W. Deng, J. Yin, X. Li and W. Guo, *Hydrovoltaic Energy from Water Droplets: Device Configurations, Mechanisms, and Applications*, Vol. 2, John Wiley and Sons Inc, 2023.
43 T. Tabrizizadeh, Z. She, K. Stamplecoskie and G. Liu, *ACS Omega*, 2022, **7**, 28275.
44 X. Liu, T. Ueki, H. Gao, T. L. Woodard, K. P. Nevin, T. Fu, S. Fu, L. Sun, D. R. Lovley and J. Yao, *Nat. Commun.*, 2022, **13**, 4369.
45 Q. Hu, Y. Ma, G. Ren, B. Zhang and S. Zhou, *Sci. Adv.*, 2022, **8**, 8047.
46 X. Li, K. Zhang, A. Nilghaz, G. Chen and J. Tian, *Nano Energy*, 2023, **112**, 108491.
47 J. Sun, P. Li, J. Qu, X. Lu, Y. Xie, F. Gao, Y. Li, M. Gang, Q. Feng, H. Liang, X. Xia, C. Li, S. Xu and J. Bian, *Nano Energy*, 2019, **57**, 269.
48 Q. Liu, J. Liang, B. Tian, E. Xue, X. Zhang, P. Guo, K. Zheng, G. Tang and W. Wu, *Small Methods*, 2023, **7**, 2300304.
49 C. Li, Z. Tian, L. Liang, S. Yin and P. K. Shen, *ACS Appl. Mater. Interfaces*, 2019, **11**, 4922.
50 D. He, Y. Yang, Y. Zhou, J. Wan, H. Wang, X. Fan, Q. Li and H. Huang, *Nano Energy*, 2021, **81**, 105630.
51 J. Zhang, P. Cui, J. Wang, H. Meng, Y. Ge, C. Feng, H. Liu, Y. Meng, Z. Zhou, N. Xuan, B. Zhang, G. Cheng and Z. Du, *Adv. Sci.*, 2023, **10**, 2304482.
52 X. Liu, H. Gao, J. E. Ward, X. Liu, B. Yin, T. Fu, J. Chen, D. R. Lovley and J. Yao, *Nature*, 2020, **578**, 550.
53 S. Chaurasia, R. Kumar, T. Tabrizizadeh, G. Liu and K. Stamplecoskie, *ACS Omega*, 2022, **7**, 2618.
54 T. Xu, X. Ding, C. Shao, L. Song, T. Lin, X. Gao, J. Xue, Z. Zhang and L. Qu, *Small*, 2018, **14**, 972–978.
55 P. Xiao, J. He, F. Ni, C. Zhang, Y. Liang, W. Zhou, J. Gu, J. Xia, S. W. Kuo and T. Chen, *Nano Energy*, 2020, **68**, 104385.
56 N. Hossain, R. Abbasi, W. Zhao, X. Zhao, A. Yu and N. Zhou, *Energy Environ. Mater.*, 2025, e70017.
57 A. B. Mamonov, R. D. Coalson, M. L. Zeidel and J. C. Mathai, *J. Gen. Physiol.*, 2007, **130**, 111.